Supplementary Information for **"Astronomical forcing shaped the timing of early Pleistocene glacial cycles"**

Yasuto Watanabe, Ayako Abe-Ouchi, Fuyuki Saito, Kanon Kino, Ryouta O'ishi, Takashi Ito, Kenji Kawamura, Wing-Le Chan

Corresponding author: Abe-Ouchi, A. (abeouchi@aori.u-tokyo.ac.jp)

Supplementary Methods

Atmosphere–Vegetation Coupled General Circulation Model MIROC–LPJ

To examine the response of climate to changes in astronomical forcings, we employ an atmosphere/slab-ocean coupled general circulation model that includes a dynamic vegetation component (MIROC-LPJ) [1–3]. The atmosphere component of MIROC-LPJ is the same as the MIROC4m Atmosphere–Ocean General Circulation Model [4], which has been used extensively for paleoclimate studies [5–7]. The AGCM of MIROC4m is based on a three-dimensional primitive equation in sigma coordinates with spectral transformation adopted for horizontal discretisation. The resolution of the atmosphere is T42 (~2.8˚×2.8˚) with 20 vertical levels. The Arakawa–Schubert scheme [8] for cumulus convection, two-stream k-distribution scheme [9] for radiation, and Mellor and Yamada [10,11] level 2 closure scheme for vertical mixing are all adopted as physical parameterisations. The land surface module, Minimal Advanced Treatment of Surface Interaction and RunOff (MATSIRO) [12], is employed as the land surface component for the AGCM, but the vegetation distribution in MATSIRO is fixed.

In MIROC–LPJ, the dynamical vegetation model is implemented as follows: the Lund-Potsdam-Jena dynamic global vegetation model (LPJ-DGVM) [13] predicts the distribution of ten vegetation types (plant functional types, PFTs) by using surface air temperature, precipitation and cloud cover fraction from the atmospheric component of MIROC. For each PFT, carbon balance is predicted from bioclimatic limits, photosynthesis, respiration, carbon allocation, plant establishment, growth, turnover, mortality, fire, and competition. Since this version of MATSIRO does not include the effect of fractional coverage of different vegetation types and just one vegetation type is represented in each grid cell, vegetation distributions represented by PFTs are translated into MATSIRO vegetation types in accordance to a conversion table in BIOME3 [2]. Finally, this MATSIRO vegetation distribution is passed onto MATSIRO annually and land surface properties are updated along with the new vegetation distribution. The seasonal change in the leaf area index (LAI) for each grid cell is prescribed with a sine curve that is defined by the maximum and minimum values for each vegetation type. All simulations in this study use a slab-ocean model, which predicts sea-surface temperature and sea-ice extent from a prescribed seasonal change in ocean heat transport, instead of a full ocean dynamic component in MIROC4m. The present-day experiment using the MIROC-LPJ coupled with a slab ocean model provides a reasonable vegetation distribution compared with the observed vegetation [14]. The MIROC-LPJ model has been validated by simulating the vegetation response to increasing pCO_2 [1], and to mid-Holocene (6 ka) [2], LGM [3], and Last Interglacial (LIG) (127 ka) [15] conditions.

The sensitivity to vegetation feedback of various orbital configurations are assessed in Ref. 16 and one example of the feedback analysis with and without vegetation feedback from this model is shown in detail in the study of the Last Interglacial experiment [15]. To isolate the impact of astronomical forcings on the climate we perform 21 experiments with the coupled MIROC-LPJ (Supplementary Table 1). These experiments incorporate idealised combinations of astronomical forcings that include the maximum and minimum values over the past 600,000 years [17]. These experiments take into account two values of the precession angle (90° and 270°), four values of eccentricity (0, 0.01671, 0.03, and 0.0493), and three values of obliquity (22.079°, 23.439°, and 24.480°) under a fixed atmospheric CO_2 concentration (230 ppm). The ice-sheet topography is fixed to present day [18] in all experiments. The simulations are run for the years shown in Table S1, and the final 50 years are used for the analyses. The model outputs are obtained at daily intervals.

The resulting surface temperature anomalies over Northern Hemisphere (NH) land are summarised in Supplementary Figure 2 [16]. The summer insolation and surface air temperature are shown as anomalies from experiment no. 11. The insolation and temperature are averaged across land areas at 50°–90°N, over 91 days centred around their respective maxima. Comparing the results with a set of experiments using the middle value of obliquity, we see that the summer temperature anomaly increases monotonically (thick grey lines in Supplementary Figure 2), which is similar to the simple relation between summer insolation and summer temperature in Abe-Ouchi et al. [6]. With three different values of obliquity (high, middle, and low) under fixed precession and eccentricity, the response of summer temperature to summer insolation is enhanced in comparison with the grey line under fixed obliquity (thin lines in Supplementary Figure 2). This effect keeps the surface temperature around 1.5 K higher/lower than expected, relative to the grey line with the middle value of fixed obliquity. The additional sensitivity due to obliquity change diminishes, especially when the anomaly of the summer temperature becomes too large (red lines in Supplementary Figure 2) and furthermore, it becomes negligibly small when the summer temperature is high. This additional sensitivity to obliquity reflects the change in the feedbacks at high latitudes, especially from vegetation (i.e. boreal forest/tundra exchange) [19,20], which is confirmed in detail by comparing the experiments with and without vegetation [16]. The differences between results in previous studies [6,19] are attributable to the shift in the high-latitude surface vegetation of the NH, and not to the choice of model [16].

We include this additional vegetation feedback from obliquity in the temperature parameterization of the ice–sheet model (Equations 1 and 2) based on our GCM experiment (Supplementary Figure 2). Estimates of the past NH surface temperature and simulated ice volumes with the inclusion of this new parameterization are compared with those using the previous configuration [5] for the last 400 kyr in Supplementary Figures 11d and 11g, respectively. The latest version of our model reproduces the glacial cycles in the last 400 kyr.

The hysteresis loop and the trajectory of the NA ice volume from MIS 5e to 1 (122–0 kyr) under a constant CO_2 (230 ppm) are shown in Supplementary Figure 7, which can be compared to the three 41-kyr glacial cycles from MIS 47 to 43 (1448–1314 ka) in Figure 6. For the last glacial cycle from MIS 5e to 1, ice-sheet retreat occurs once in every four or five precession cycles when the ice sheet grows sufficiently to trigger deglaciation (Supplementary Figures 7a and 7d). This is because the astronomical forcing is not sufficiently large to trigger deglaciation since eccentricity remains small for two or three precession cycles during the development of the NH ice sheet (e.g., from MIS 4 to 2) [5].

Surface temperature anomaly from MIS 53 to 36

The surface temperature anomaly due to variations in insolation (ΔT_{sol}) before the MPT, as calculated from the variations in astronomical forcings [17], is shown in Supplementary Figure 9f. The ~20-kyr and 41-kyr spectral power of the resulting ΔT_{sol} are almost comparable to one another and they are close to that of the caloric summer half-year insolation [21,22] (Supplementary Figure 10d) and the integrated summer insolation [23] (Supplementary Figure 10e) at 65°N, both calculated using the *palinsol* software package [24]. The vegetation feedback on NA surface temperature [1–3,19] may be the physical mechanism that explains why these sets of insolation are good predictors of deglaciations in the Quaternary [22]. The surface temperature anomaly calculated using this ΔT_{sol} variation and three different pCO_2 configurations before the MPT is shown in Supplementary Figure 10g. Using this surface temperature anomaly as input for the IcIES ice-sheet model, we examine the response of the NH ice sheet under realistic astronomical forcings.

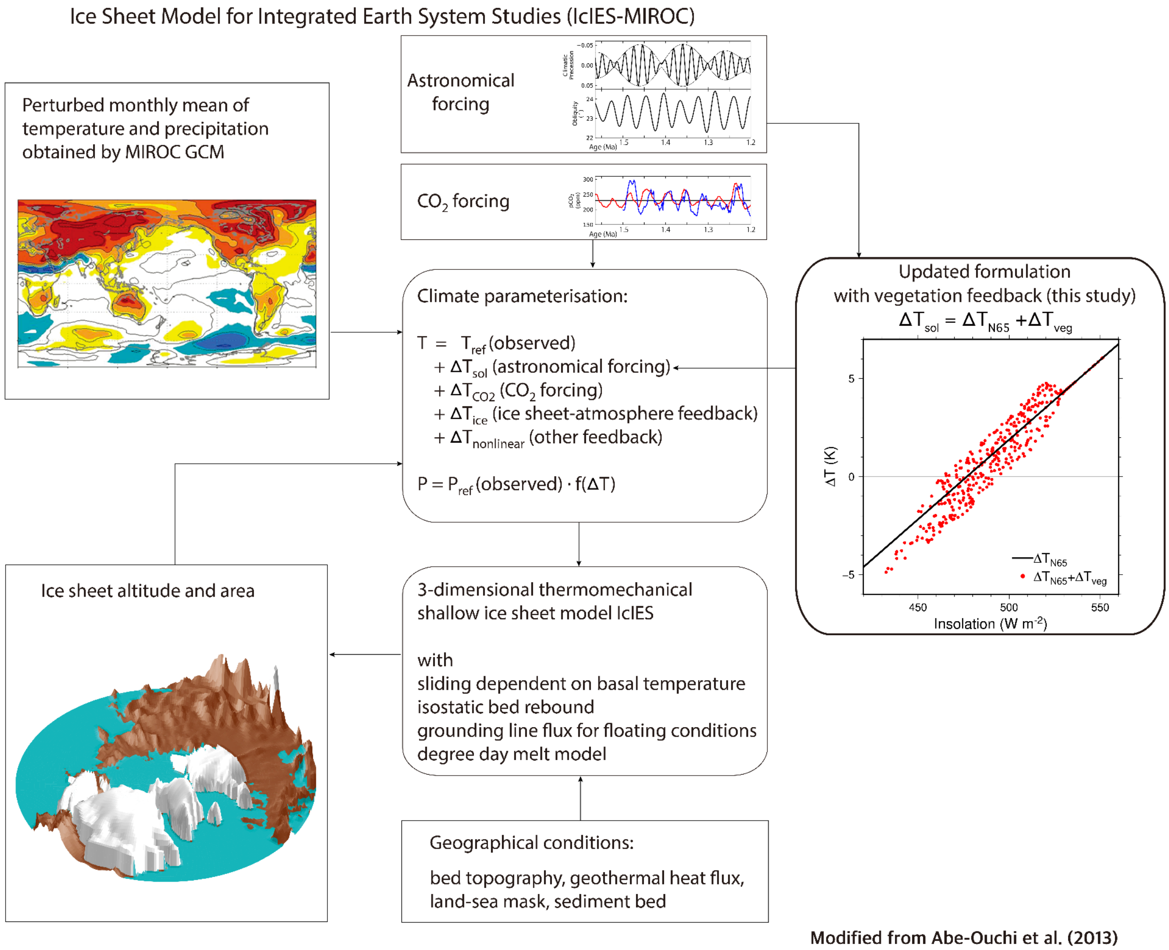

Supplementary Figure 1. Schematic illustration of the IcIES-MIROC model. The original figure is from the Supplementary Materials of Abe-Ouchi et al. (2013) [5]. The variations of the astronomical forcing are from Berger and Loutre [17]. The variations of atmospheric pCO_2 forcing are from van de Wal et al. [25] (red line) and Lisiecki [26] (blue line). The figure is modified to illustrate the updated formulation which considers the vegetation feedback in this study (right panel with a thick frame). The black line represents the temperature parameterization in the previous study by Abe-Ouchi et al. (2013) [5]. The red dots represent the improved temperature parameterization for every 1 kyr at 1565–1200 ka. The range of the red dots compared with the black line represents the vegetation feedback estimated in this study.

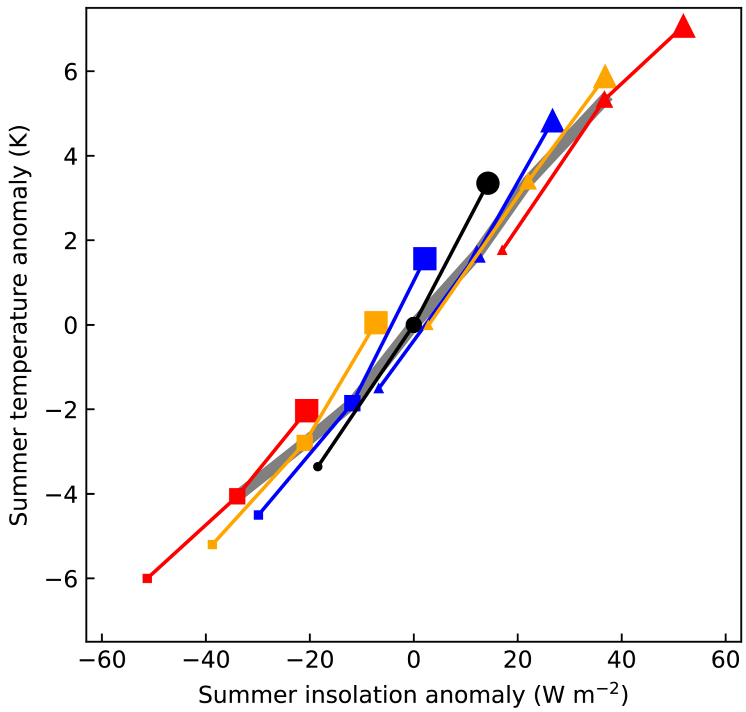

Supplementary Figure 2. Relationship between summer insolation anomaly and summer temperature anomaly with vegetation feedback based on MIROC-LPJ.

Colours correspond to eccentricity (black: 0.00, blue: 0.01671, orange: 0.03, red: 0.0493). Markers correspond to precession angle (circle: undefined, triangle: 270°, rectangle: 90°). The size of each marker corresponds to obliquity (small: 22.079°, middle: 23.439°, large: 24.480°).

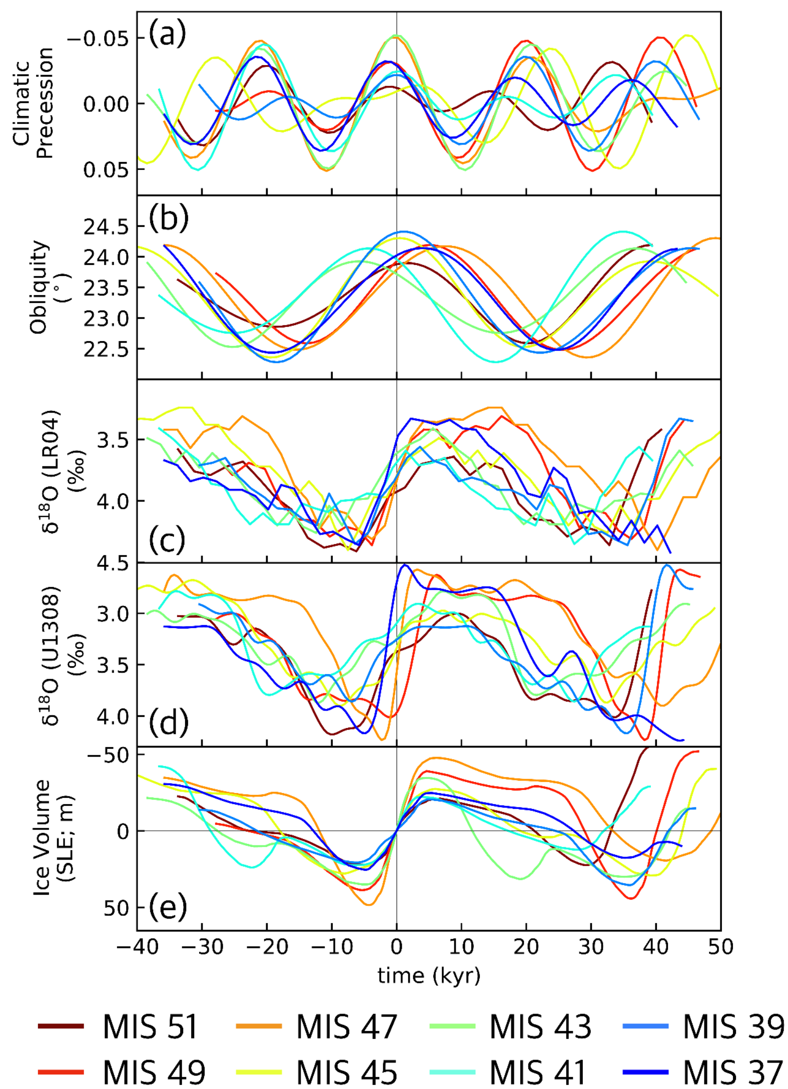

Supplementary Figure 3. Simulated time series of forcing and the response of Northern Hemisphere ice sheets for each set of two glacial cycles aligned at the timing of the simulated deglaciation.

Time axis and modelled sea level equivalent (SLE) of ice volume change under a constant CO_2 concentration of 230 ppm shown as the deviation from the defined timings of deglaciations: (a) Climatic precession [17]. (b) Obliquity [17]. (c–d) $\delta^{18}O$ signature from Lisiecki and Raymo [27] and U1308 core [28], respectively. Data from U1308 core [28] are filtered using a zero-phase low-pass Butterworth filter. (e) Simulated Northern Hemisphere ice sheet volume (unit: m, sea level equivalent; SLE) across each deglaciation, relative to the ice volume at each deglaciation. The Marine Isotope stage (MIS) number represents the interglacial after each deglaciation.

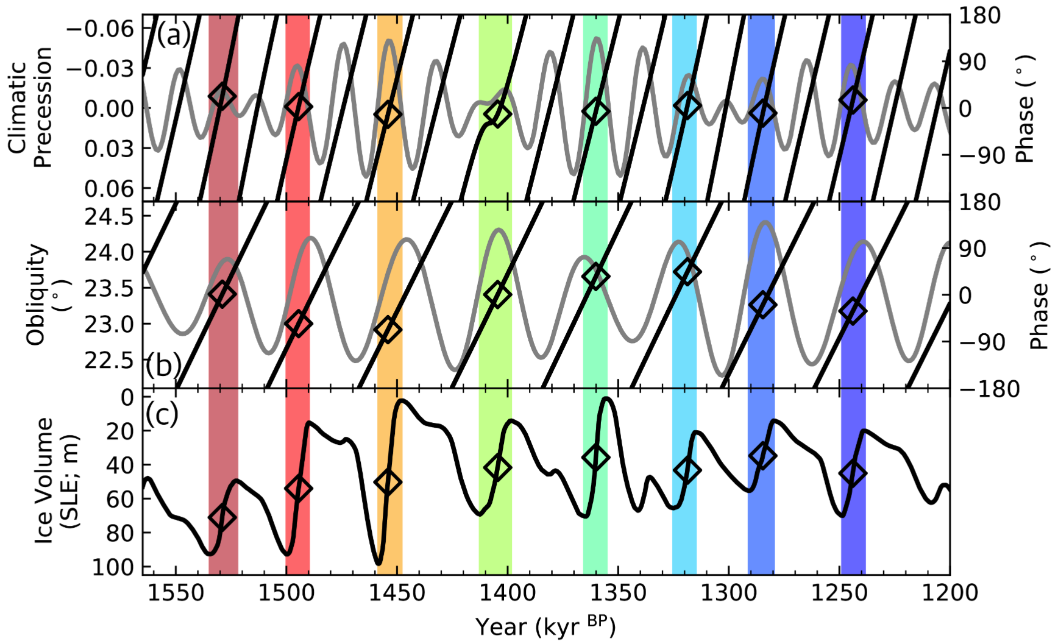

Supplementary Figure 4. Relationship between the simulated deglaciation and phase angle of astronomical forcings.

(a–b) Time series (grey) [17] and phase angles (black) of climatic precession and obliquity, respectively. When the phase is positive, the peak strength of astronomical forcings precedes the timing of deglaciation. When the phase is negative, the timing of deglaciation precedes the peak strength of astronomical forcings. (c) Simulated Northern Hemisphere ice sheet volume (unit: m, sea level equivalent; SLE) under a fixed CO_2 forcing of 230 ppm (black line) and defined timings of deglaciations (diamonds and coloured shading).

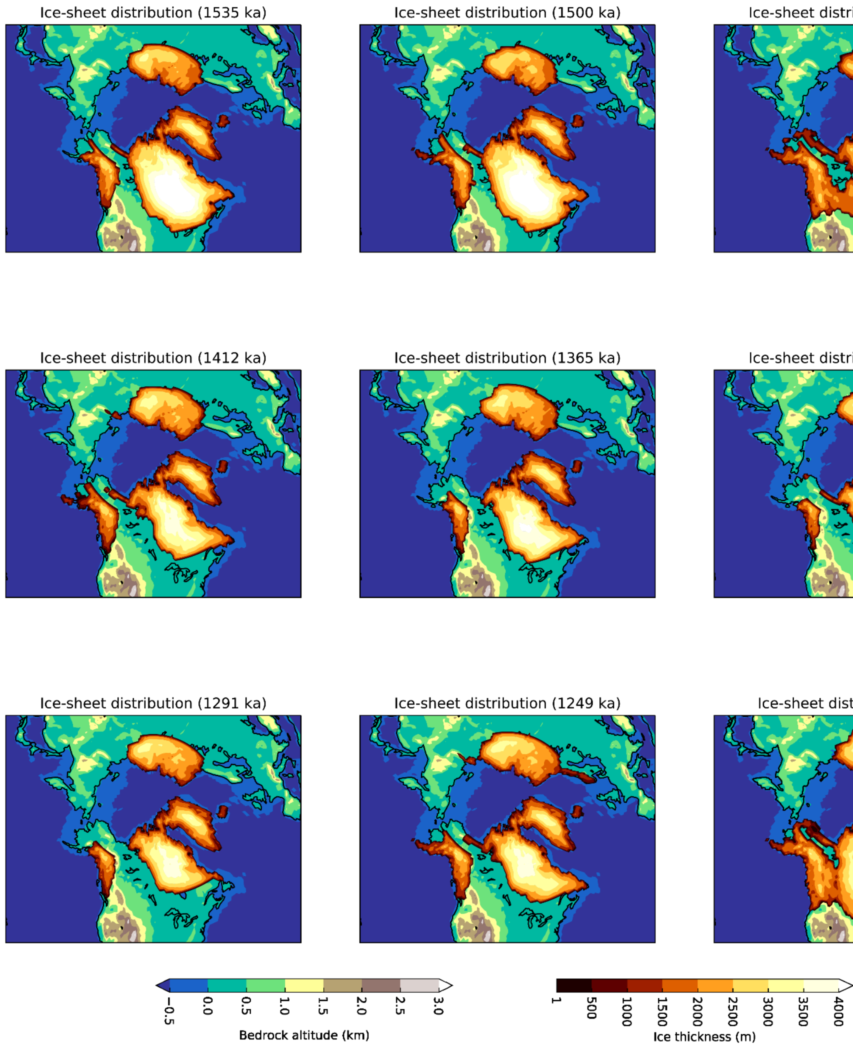

Supplementary Figure 5. Simulated ice-sheet distribution for all glacial periods. (A–H) Simulated North American ice sheet distribution for each glacial maximum from Marine Isotope Stage (MIS) 52 to MIS 38 under a constant CO_2 concentration of 230 ppm and MIS 2 (LGM, 21 kyr ^{BP}) under variable atmospheric pCO_2.

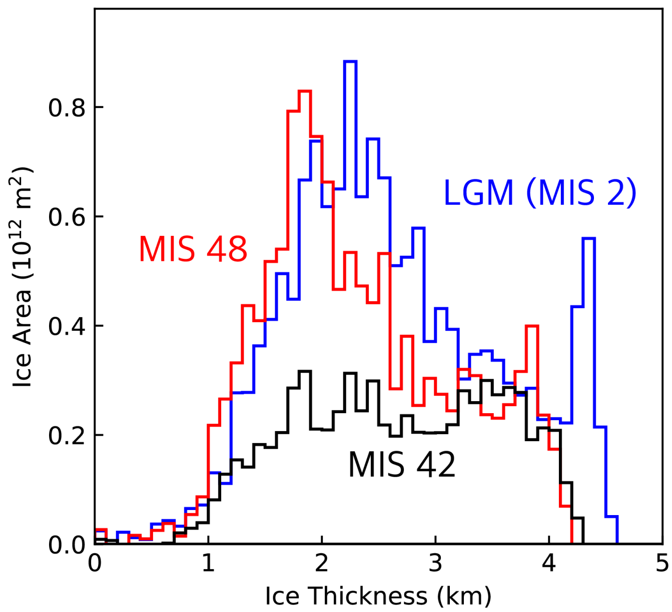

Supplementary Figure 6. Histograms of the North American Ice Sheet thickness at Marine Isotope Stage (MIS) 48, 42, and 2 (Last Glacial Maximum, LGM). The distributions of the MIS 48 and 42 are derived from our calculation under a constant CO_2 concentration of 230 ppm as in Supplementary Figure 5. The distribution of the LGM ice sheet is derived from our calculation under a realistic variation in pCO_2.

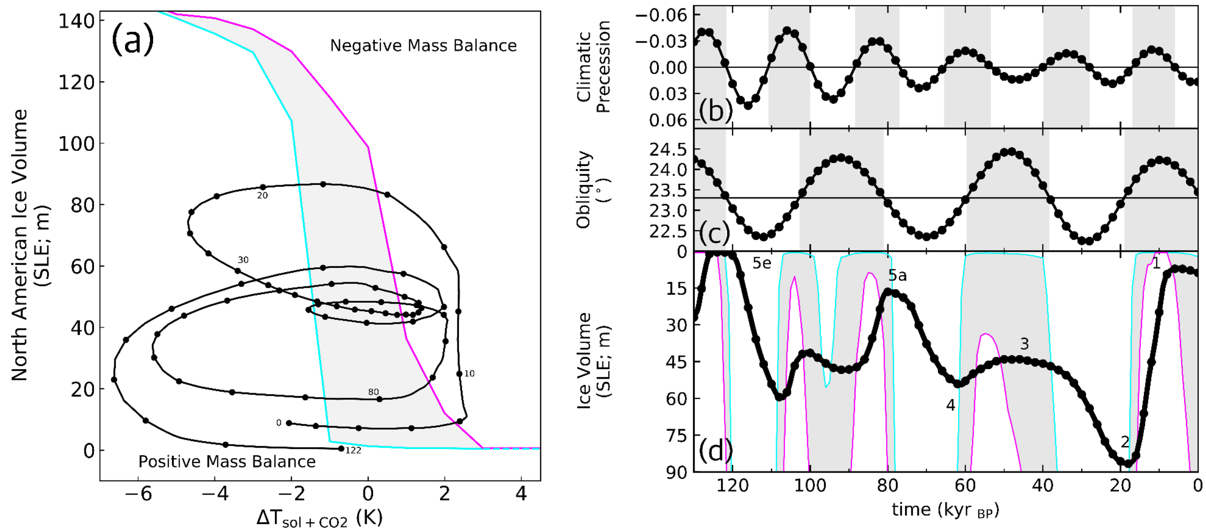

Supplementary Figure 7. Hysteresis of steady states and transient evolution of the North American ice sheet for the simulated last glacial cycle using IcIES–MIROC.

Magenta/cyan lines denote large/small volume steady states when the model run starts with large/small initial ice sheets [5]. (a) Plot showing equilibrium shapes and surface mass balances of ice sheets according to temperature anomalies relative to the present value. Lines with dots at 2-kyr intervals represent the transient evolution of the ice volume from Marine Isotope Stage (MIS) 5e to 1 (black), which is calculated under a constant $p\mathrm{CO}_2$ of 230 ppm. (b–d) Time evolution of climatic precession, obliquity, and North American ice sheet volume (unit: m, sea level equivalent; SLE), respectively. Grey shading represents periods when precession is below average or when obliquity is above average.

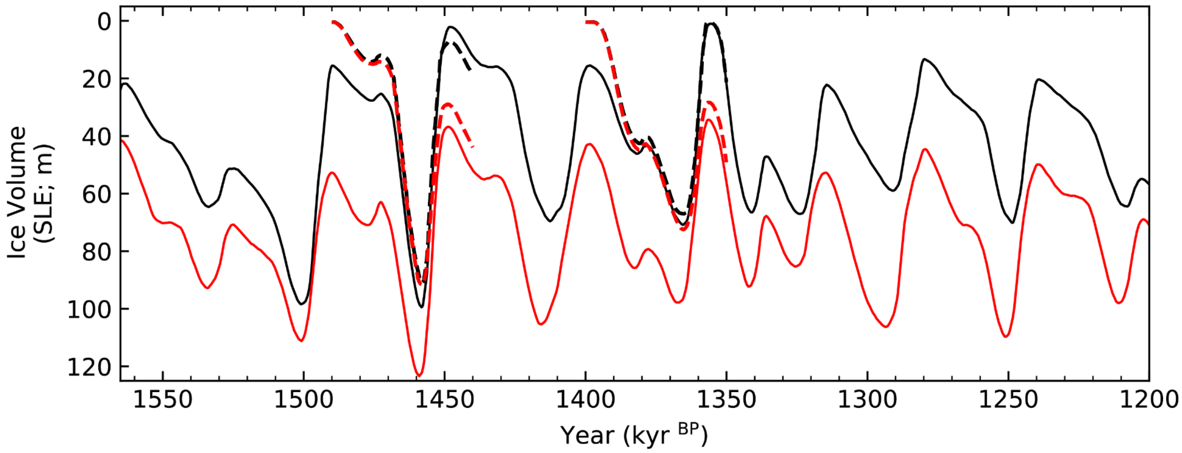

Supplementary Figure 8. Influence of the time constants for the isostatic rebound on the simulated ice sheet volume of IcIES–MIROC.

Simulated Northern Hemisphere ice sheet volume (unit: m, sea level equivalent; SLE) with two different time constants, τ, for isostatic rebound: 5000 years (standard, shown by black lines) and 1 year (red lines), calculated under 230 ppm pCO_2. Initial conditions are fixed at 1.6 Ma for long calculations from 1.6 to 1.2 Ma (solid lines). Calculations using initial conditions fixed at each interglacial level (ice volume: ~ 0 m) are also conducted for one glacial cycle from Marine Isotope Stage (MIS) 49 to 47 and from MIS 45 to 43 under 230 ppm pCO_2 (dashed lines).

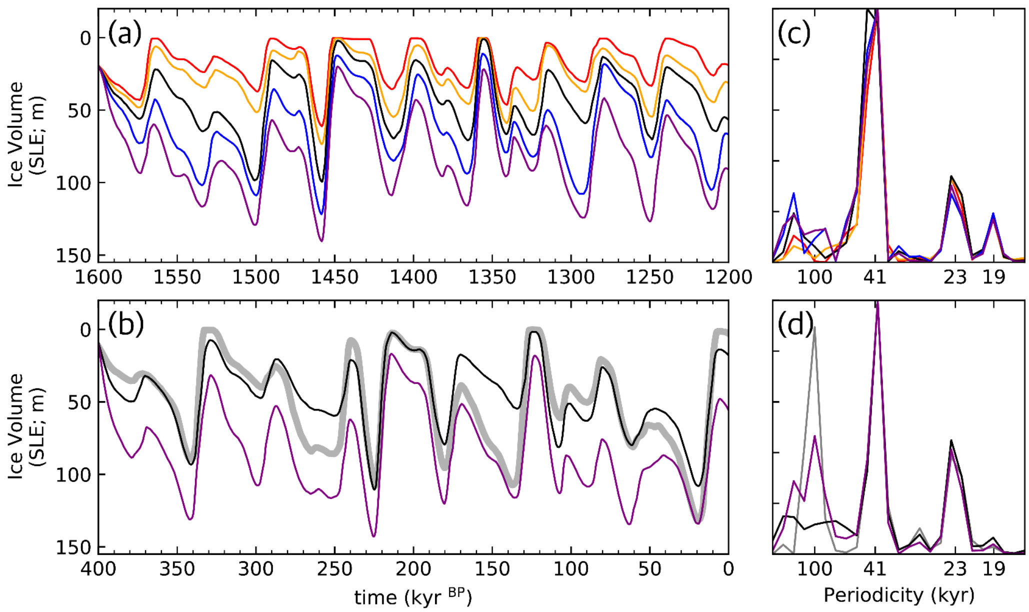

Supplementary Figure 9. Simulated Time series of forcing and the response of Northern Hemisphere ice sheets under different constant $p\mathrm{CO_2}$ inputs.

(a–b) Time series of the period of interest, and (c–d) corresponding normalised amplitude spectra, respectively: (a) Simulated Northern Hemisphere ice sheet volume (unit: m, sea level equivalent; SLE) calculated with a constant atmospheric $p\mathrm{CO_2}$ of 190 (purple), 210 (blue), 230 (black) 250 (orange), and 270 ppm (red) from 1.6 to 1.2 Ma and (b) 190 (purple), 230 (black), and the simulation with variable $p\mathrm{CO_2}$ based on ice core reconstruction [29] (grey) for the last 400 kyr. As the calculations in (a) start from 1.6 Ma, the calculation with 230 ppm in this figure differs from the standard 230 ppm run.

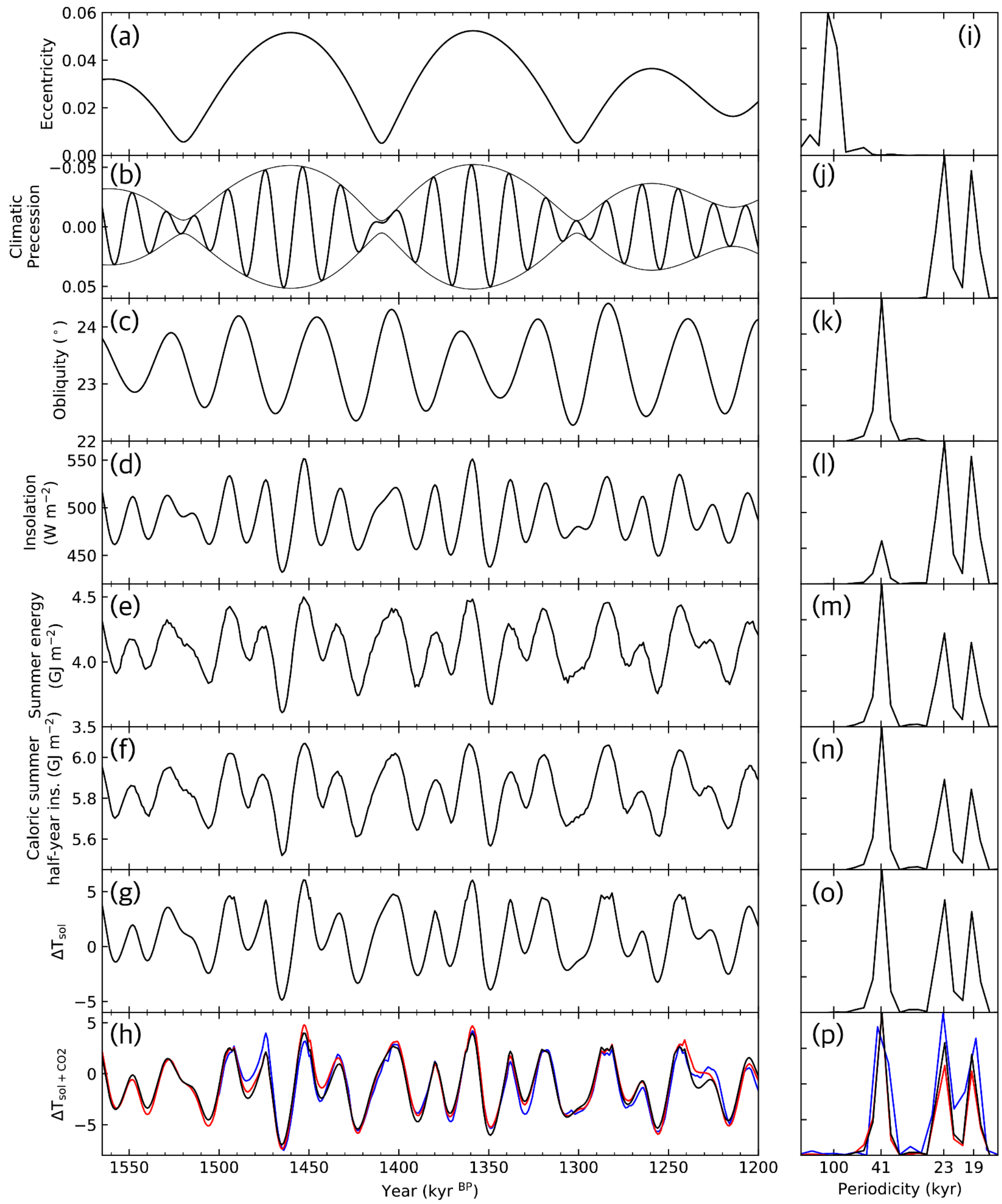

Supplementary Figure 10. Time series of astronomical forcings, various summer insolations, and calculated surface temperature used in the experiments of IcIES–MIROC. (a–h) Time series of the period of interest and (i–p) corresponding normalised amplitude spectra, respectively: (a) Eccentricity [17]. (b) Climatic precession [17]. (c) Obliquity [17]. (d) Insolation at 65°N on June 21 [17]. (e–f) Caloric summer half-year insolation at 65°N [22] (GJ m^{-2}) (e) and the summer energy [23] (GJ m^{-2}) (f) calculated using *Palinsol* [24]. (g) Surface temperature anomaly, ΔT_{sol} (K), derived in this study. (h) Surface temperature anomalies due to insolation and CO_2 forcing, ΔT_{sol} + ΔT_{CO2}, respectively (black: constant value of 230 ppm, red: van de Wal et al. [25], blue: Lisiecki [26]).

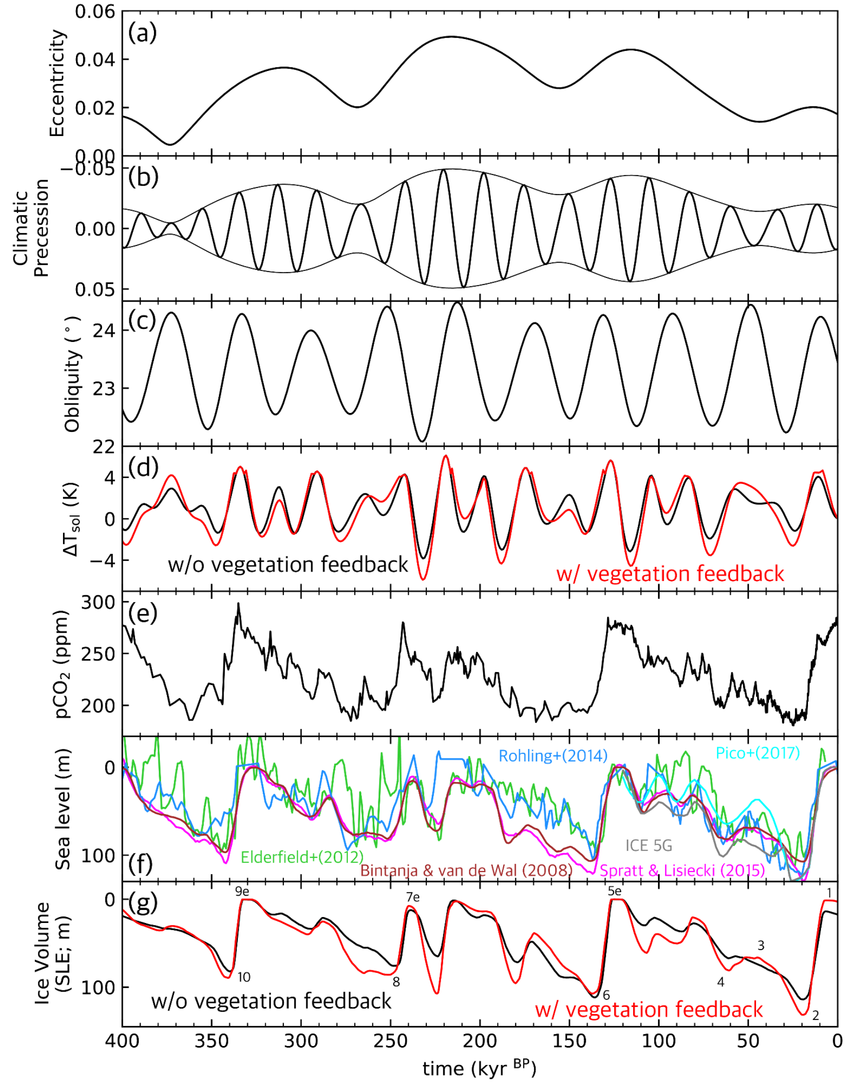

Supplementary Figure 11. Updated forcing and the simulated response of the North American ice sheet under revised surface temperature anomalies for the last 400 kyr.

(a) Eccentricity [17]. (b) Climatic precession [17]. (c) Obliquity [17]. (d) Surface temperature anomaly computed with Equation 2 with/without the inclusion of additional surface temperature anomaly ΔT_{veg} (red/black). (e) Reconstructions of past atmospheric pCO_2 (Bereiter et al. [29]). (f) Reconstructions of past sea level elevation. Brown: Bintanja and van de Wal. [30], green: Elderfield et al. [31], magenta: LR04 curve [27] converted to sea level based on Spratt and Lisiecki [32], blue: Rohling et al. [33], cyan: Pico et al. [34], gray: ICE-5G [35]. (g) Simulated Northern Hemisphere ice sheet volume (unit: m, sea level equivalent; SLE) for the last 400 kyr. The black and red lines correspond to the simulations with and without consideration of the additional surface temperature anomalies due to the vegetation feedback (ΔT_{veg}), respectively. These calculations are conducted with a realistic variation in pCO_2 [29].

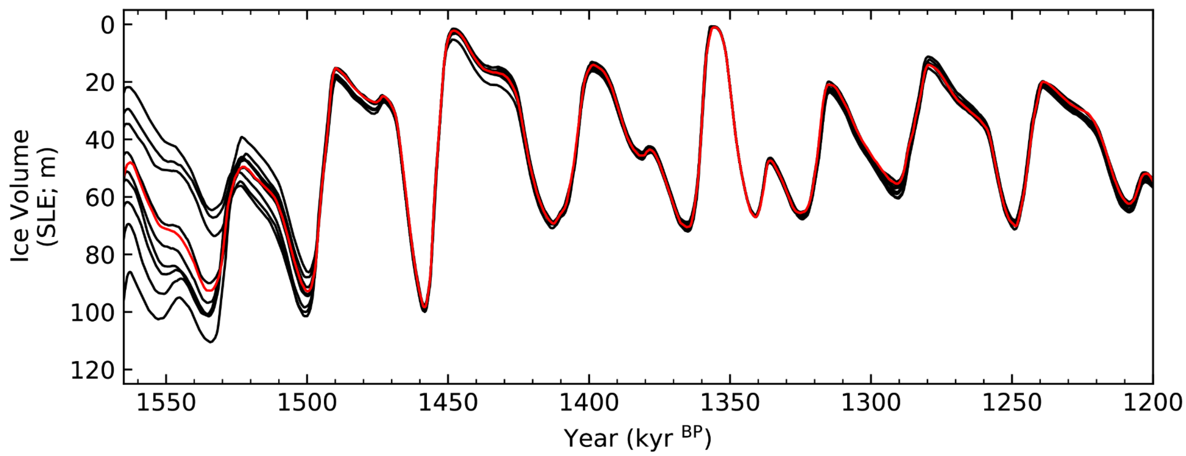

Supplementary Figure 12. Dependence of the simulated ice sheet volume on initial conditions.

Simulated Northern Hemisphere ice sheet volume (unit: m, sea level equivalent; SLE). Calculations are conducted with a fixed $p\mathrm{CO}_2$ of 230 ppm with different initial conditions. Red line corresponds to the control experiment adopted in the main text.

Supplementary Table 1. List of time slice experiments using MIROC-LPJ AGCM and the setup of the astronomical forcing, atmospheric pCO_2, and the number of years of integration.

	H (High)	M (Middle)	L (Low)	0
Obliquity (°)	24.480	23.439	22.079	-
Eccentricity	0.0493	0.03	0.01671	0

	SS (Summer solstice)	WS (Winter solstice)
Precession angle (°)	270	90

No.	Orbital parameters			CO_2	Integrated
	Precession	Eccentricity	Obliquity	(ppm)	year
1	SS	H	H	230	480
2	SS	H	M	230	420
3	SS	H	L	230	420
4	SS	M	H	230	490
5	SS	M	M	230	420
6	SS	M	L	230	420
7	SS	L	H	230	390
8	SS	L	M	230	450
9	SS	L	L	230	450
10	-	0	H	230	630
11	-	0	M	230	360
12	-	0	L	230	420
13	WS	H	H	230	390
14	WS	H	M	230	390
15	WS	H	L	230	390
16	WS	M	H	230	560
17	WS	M	M	230	390
18	WS	M	L	230	390
19	WS	L	H	230	390
20	WS	L	M	230	390
21	WS	L	L	230	390

Supplementary Table 2. Summary of the characteristics of each simulated glacial cycle in terms of the length of glacial and interglacial periods, glacial ice extent, and the shape of the glacial cycle. $\Phi_{PRE-OBL}$ represents the relative phase angle of obliquity at the beginning of the cycle. The values are obtained from our standard run, which is forced with a constant CO_2 fixed at 230 ppm.

MIS stage	Initiation of an interglacial period (ka)	Initiation of a glacial period (ka)	Interglacial duration (kyr)	Glacial duration (kyr)	Shape of glacial cycle	$\Phi_{PRE-OBL}$ at a previous deglaciation (°)
53–52	–	1551.9	–	22.9	–	–
51–50	1529.0	1507.5	21.5	13.0	Sawtoothed	+1.3474
49–48	1494.5	1465.2	29.3	11.1	Plateau-like	–55.53
47–46	1454.1	1423.5	30.6	19.0	Plateau-like	–67.164
45–44	1404.5	1385.0	19.5	24.9	Sawtoothed	+0.54071
43–42	1360.1	1348.7	11.4	30.0	Triangular peak-like	+35.477
41–40	1318.7	1304.3	14.4	19.7	Triangular peak-like	+44.451
39–38	1284.6	1257.2	27.4	13.3	Sawtoothed	–19.232
37–36	1243.9	1217.7	26.2	–	Plateau-like	–31.341

Supplementary References

1. O'ishi, R. & Abe-Ouchi, A. Influence of dynamic vegetation on climate change arising from increasing CO2. *Clim. Dyn.* **33**, 645–663 (2009).
2. O'ishi, R. & Abe-Ouchi, A. Polar amplification in the mid-Holocene derived from dynamical vegetation change with a GCM. *Geophys. Res. Lett.* **38**, (2011).
3. O'ishi, R. & Abe-Ouchi, A. Influence of dynamic vegetation on climate change and terrestrial carbon storage in the Last Glacial Maximum. *Clim. Past* **9**, 1571–1587 (2013).
4. K-1 Model Developers. *K-1 Coupled GCM (MIROC) Description*. vol. K-1 Technical Report 1 1–34 (2004).
5. Abe-Ouchi, A. *et al.* Insolation-driven 100,000-year glacial cycles and hysteresis of ice-sheet volume. *Nature* **500**, 190–193 (2013).
6. Abe-Ouchi, A., Segawa, T. & Saito, F. Climatic conditions for modelling the Northern Hemisphere ice sheets throughout the ice age cycle. *Clim. Past* **3**, 423–438 (2007).
7. Kawamura, K. *et al.* State dependence of climatic instability over the past 720,000 years from Antarctic ice cores and climate modeling. *Science Advances* **3**, e1600446 (2017).
8. Arakawa, A. & Schubert, W. H. Interaction of a cumulus cloud ensemble with the large-scale environment, Part I. *J. Atmos. Sci.* (1974).
9. Nakajima, T. & Tanaka, M. Matrix formulations for the transfer of solar radiation in a plane-parallel scattering atmosphere. *J. Quant. Spectrosc. Radiat. Transf.* **35**, 13–21 (1986).
10. Mellor, G. L. & Yamada, T. A hierarchy of turbulence closure models for planetary boundary layers. *J. Atmos. Sci.* (1974).
11. Mellor, G. L. & Yamada, T. Development of a turbulence closure model for geophysical fluid problems. *Rev. Geophys.* **20**, 851 (1982).
12. Takata, K., Emori, S. & Watanabe, T. Development of the minimal advanced treatments of surface interaction and runoff. *Glob. Planet. Change* **38**, 209–222 (2003).
13. Sitch, S. *et al.* Evaluation of ecosystem dynamics, plant geography and terrestrial carbon cycling in

the LPJ dynamic global vegetation model. *Glob. Chang. Biol.* **9**, 161–185 (2003).

14. Ramankutty, N. & Foley, J. A. Estimating historical changes in global land cover: Croplands from 1700 to 1992. *Global Biogeochem. Cycles* **13**, 997–1027 (1999).
15. O'ishi, R. *et al.* PMIP4/CMIP6 last interglacial simulations using three different versions of MIROC: importance of vegetation. *Clim. Past* **17**, 21–36 (2021).
16. Kino, K. *Feedback analyses of the seasonality of polar climate change driven by changes in the orbital parameters [in Japanese]*. (Msc thesis, The University of Tokyo, 2017).
17. Berger, A. & Loutre, M. F. Insolation values for the climate of the last 10 million years. *Quaternary Science Reviews* **10**, 297–317 (1991).
18. Peltier, W. R. Global glacial isostasy and the surface of the ice-age Earth: the ICE-5G (VM2) model and GRACE. *Annu. Rev. Earth Planet. Sci.* **32**, 111–149 (2004).
19. Tabor, C. R., Poulsen, C. J. & Pollard, D. Mending Milankovitch's theory: obliquity amplification by surface feedbacks. *Clim. Past* **10**, 41–50 (2014).
20. Bounceur, N., Crucifix, M. & Wilkinson, R. D. Global sensitivity analysis of the climate–vegetation system to astronomical forcing: an emulator-based approach. *Earth Syst. Dyn.* **6**, 205–224 (2015).
21. Milankovitch, M. *Kanon der Erdbestrahlung und Seine Anwendung auf das Eiszeit-Problem*. (R. Serbian Acad., Belgrade, Serbia, 1941).
22. Tzedakis, P. C., Crucifix, M., Mitsui, T. & Wolff, E. W. A simple rule to determine which insolation cycles lead to interglacials. *Nature* **542**, 427–432 (2017).
23. Huybers, P. Early Pleistocene Glacial Cycles and the Integrated Summer Insolation Forcing. *Science* **313**, 508–511 (2006).
24. Crucifix, M. *Palinsol: insolation for palaeoclimate studies, R package*. (2016).
25. van de Wal, R. S. W., de Boer, B., Lourens, L. J., Köhler, P. & Bintanja, R. Reconstruction of a continuous high-resolution CO_2 record over the past 20 million years. *Clim. Past* **7**, 1459–1469 (2011).
26. Lisiecki, L. E. A benthic δ13C-based proxy for atmospheric pCO2 over the last 1.5 Myr. *Geophys.*

Res. Lett. **37**, (2010).

27. Lisiecki, L. E. & Raymo, M. E. A Pliocene-Pleistocene stack of 57 globally distributed benthic δ18O records. *Paleoceanography* **20**, (2005).
28. Hodell, D. A. & Channell, J. E. T. Mode transitions in Northern Hemisphere glaciation: co-evolution of millennial and orbital variability in Quaternary climate. *Clim. Past* **12**, 1805–1828 (2016).
29. Bereiter, B. *et al.* Revision of the EPICA Dome C CO2 record from 800 to 600 kyr before present. *Geophys. Res. Lett.* **42**, 542–549 (2015).
30. Bintanja, R. & van de Wal, R. S. W. North American ice-sheet dynamics and the onset of 100,000-year glacial cycles. *Nature* **454**, 869–872 (2008).
31. Elderfield, H. *et al.* Evolution of ocean temperature and ice volume through the mid-Pleistocene climate transition. *Science* **337**, 704–709 (2012).
32. Spratt, R. M. & Lisiecki, L. E. A Late Pleistocene sea level stack. *Clim. Past* **12**, 1079–1092 (2016).
33. Rohling, E. J. *et al.* Sea-level and deep-sea-temperature variability over the past 5.3 million years. *Nature* **508**, 477–482 (2014).
34. Pico, T., Creveling, J. R. & Mitrovica, J. X. Sea-level records from the U.S. mid-Atlantic constrain Laurentide Ice Sheet extent during Marine Isotope Stage 3. *Nat. Commun.* **8**, 15612 (2017).
35. Peltier, W. R. & Fairbanks, R. G. Global glacial ice volume and Last Glacial Maximum duration from an extended Barbados sea level record. *Quat. Sci. Rev.* **25**, 3322–3337 (2006).